PAMM
Proceedings in Applied
Mathematics and Mechanics

RESEARCH ARTICLE

Investigation of microstructure evolution accounting for crystal plasticity in the multiphase-field method

Thea Kannenberg[1,2] | Lukas Schöller[1,2] | Andreas Prahs[1] | Daniel Schneider[2,3] | Britta Nestler[1,2,3]

[1]Institute for Applied Materials—Microstructure Modelling and Simulation (IAM-MMS), Karlsruhe Institute of Technology (KIT), Karlsruhe, Germany

[2]Institute of Digital Materials Science (IDM), Karlsruhe University of Applied Sciences, Karlsruhe, Germany

[3]Institute of Nanotechnology (INT), Karlsruhe Institute of Technology (KIT), Eggenstein-Leopoldshafen, Germany

Correspondence
Thea Kannenberg, Institute for Applied Materials—Microstructure Modelling and Simulation (IAM-MMS), Karlsruhe Institute of Technology (KIT), Straße am Forum 7, 76131 Karlsruhe, Germany.
Email: thea.kannenberg@h-ka.de

Abstract
Regarding microstructured materials, a quantitative prediction of phase transformation processes is highly desirable for a wide range of applications. With respect to polycrstalline materials, the plastic material behavior is commonly investigated using a crystal plasticity (CP) theory, since it accounts for the underlying microstructure, that is, slip systems of the crystal lattice. In classical continuum mechanics, grain boundaries (GBs) are commonly modeled as material singular surfaces. However, the tracking of moving GBs, present during phase transformation processes, is numerically challenging and costly. This can be circumvented by the use of a multiphase-field method (MPFM), which provides a numerically highly efficient method for the treatment of moving interfaces, considered as diffuse interfaces of finite thickness. In this work, the microstructural evolution is investigated within the MPFM accounting for CP. The implementation of the constitutive material behavior within the diffuse interface region accounts for phase-specific plastic fields and the jump condition approach. To improve the understanding of the impact of plastic deformation on the phase evolution, a single inclusion problem is analyzed. Within a plastically deformed matrix, the shape evolution of a purely elastic inclusion with a different Young's modulus, referred to as inhomogeneity, is investigated. It is shown, how the anisotropic plastic behavior affects the phase evolution. The resulting equilibrium shapes are illustrated and examined.

1 | INTRODUCTION

The investigation of microstructural evolution of crystalline materials is an important objective in materials science. Simulations of the evolution help to gain insights into material behavior and underlying mechanisms. For a wide range of applications, a quantitative prediction of phase transformation processes in microstructured materials is highly desirable. In classical continuum mechanics, grain boundaries (GBs) are commonly modeled as material singular surfaces [1], representing sharp interfaces. The tracking of these sharp interfaces during a microstructure evolution is associated with a high numerical expense. The multiphase-field method (MPFM) provides a numerically efficient treatment of evolving surfaces,
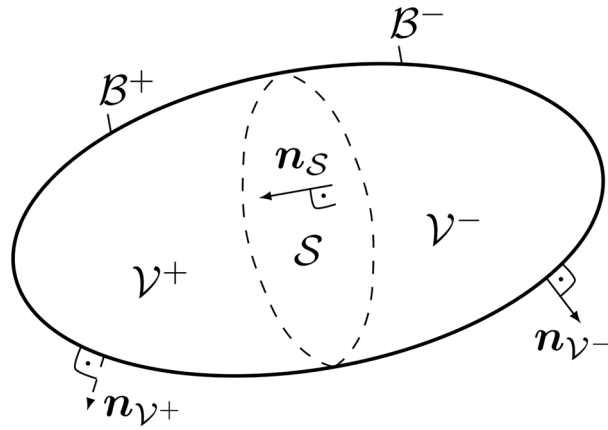
FIGURE 1 Schematic illustration of a material volume $\mathcal{V}$, which is divided by a material singular surface $\mathcal{S}$ into two subvolumes $\mathcal{V}^+$ and $\mathcal{V}^-$.

since these are considered as diffuse interfaces of finite thickness and their position is given implicitly by the contour of the phase-field order parameters, compare, for example, Refs. [2–4]. The plastic material behavior of polycrystalline materials at the micrometer scale is commonly investigated using a crystal plasticity (CP) theory, compare Asaro [5]. It accounts for the underlying microstructure, that is, slip systems of the crystal lattice. With the incorporation of CP theory in an MPFM, new possibilities arise in the quantitative modeling of solid–solid phase transformation processes that involve plasticity. Different approaches on how to deal with mechanical fields in the diffuse interface have been developed, for example, interpolation approaches, homogenization approaches, and a jump condition approach, compare Refs. [6, 7].

The implementation of the constitutive material behavior within the diffuse interface region, as used in the work at hand, accounts for phase-specific plastic fields, compare, for example, Herrmann et al. [8] and the jump condition approach, compare, for example, Refs. [9–11]. The corresponding implementation of the CP theory within the MPFM approach is introduced and discussed by Prahs et al. [12]. The coupling between the multiphase-field evolution equation and the balance of linear momentum is realized with a staggered scheme. The balance of linear momentum is solved by means of the finite element analysis. In order to investigate the possibilities of the staggered coupling regarding the modeling of GB migration, the shape evolution of an elastic inhomogeneity within a plastically deformed matrix under the influence of an external load is investigated.

2 | BALANCE LAWS AND CONSTITUTIVE EQUATIONS

Balance laws

Subsequently, a Cauchy–Boltzmann continuum is considered, which is divided into the subvolumes $\mathcal{V}^+$ and $\mathcal{V}^-$ by a material singular surface $\mathcal{S}$, as illustrated in Figure 1. The subvolumes are bounded against the surroundings by $\mathcal{B}^+$ and $\mathcal{B}^-$. The normal vector $\boldsymbol{n}_\mathcal{S}$ on $\mathcal{S}$ points from $\mathcal{V}^-$ to $\mathcal{V}^+$ and the outward normal vectors on $\mathcal{B}^+$ and $\mathcal{B}^-$ are written as $\boldsymbol{n}_{\mathcal{V}+}$ and $\boldsymbol{n}_{\mathcal{V}-}$, respectively.

The validity of the relation between the normal vectors $\boldsymbol{n}_\mathcal{S} = \boldsymbol{n}_{\mathcal{V}+} = -\boldsymbol{n}_{\mathcal{V}-}$ is given by the pill box theorem, compare, for example, Liu [13]. A jump across $\mathcal{S}$ of a quantity ψ is defined as $[\![\psi]\!] = \psi^+ - \psi^-$, where ψ^+ and ψ^- denote the corresponding limits in $\mathcal{V}^+$ and $\mathcal{V}^-$, respectively. For the above described continuum, it can be shown that the balance equations at the singular surface and in regular points are derived by exploiting the invariance of the balance of total energy with respect to a change of observer. Moreover, the existence of the stress tensor $\boldsymbol{\sigma}$, the Cauchy stress, with $\boldsymbol{\sigma}\boldsymbol{n}_\mathcal{V} = \boldsymbol{t}$ is obtained by exploiting invariance considerations. The traction force is referred to as $\boldsymbol{t}$. A detailed discussion on the derivation for regular points is provided, for example, by Svendsen [14] and Prahs and Böhlke [1], and by Prahs and Böhlke [15] for singular points. In this work, a small deformation framework is considered, implying a constant mass density. Moreover, body forces are neglected, and the quasi static case is considered. With these assumptions at hand, regarding regular points, the balance of linear momentum is given by $\mathrm{div}(\boldsymbol{\sigma}) = \boldsymbol{0}$. The symmetry of the Cauchy stress tensor follows the balance of angular momentum in regular points, $\boldsymbol{\sigma} = \boldsymbol{\sigma}^\mathsf{T}$. The continuity of the stress tensor across $\mathcal{S}$ in the normal direction is defined by the simplified balance of linear momentum on $\mathcal{S}$, reading $[\![\boldsymbol{t}]\!] = \boldsymbol{0}$.

Hadamard conditions

For a jump across a singular surface $\mathcal{S}$ additional conditions hold, for example, the Hadamard jump condition $\{F\} = a \otimes n_{\mathcal{S}}$, compare, for example, Liu [13]. Herein, a denotes an unknown jump vector and the deformation gradient is written as F. While the balance of linear momentum at the singular surface states the continuity of the stress tensor in the normal direction of $\mathcal{S}$, the Hadamard condition states the continuity of the deformation gradient tangential to $\mathcal{S}$. Taking into account the definition of F in terms of the displacement gradient H and the second-order identity tensor I, that is, $F = H - I$, the Hadamard condition is reformulated as $\{H\} = a \otimes n_{\mathcal{S}}$.

Constitutive equations of CP

The classical CP theory, compare, for example, Asaro [5], describes the plastic deformation entirely in terms of the plastic slips and, thus, represents a phenomenological plasticity theory. It accounts for the underlying crystalline microstructure, the crystal lattice, and its slip systems. Since a small deformation framework is considered, it is assumed that the total strain ε can be additively composed of an elastic ε_e and a plastic contribution ε_p. The relation between the elastic strain ε_e and the Cauchy stress σ is given by Hookes law, that is,

$$\varepsilon = \varepsilon_e + \varepsilon_p, \qquad \sigma = \mathbb{C}[\varepsilon_e] = \mathbb{C}[\varepsilon - \varepsilon_p]. \tag{1}$$

The deformation of a crystal corresponds to the stretching and rotation of the lattice vectors, compare, for example, [5]. Defining a slip system, the slip direction d_ξ and a normal vector n_ξ to the slip plane can be considered as lattice vectors. Face-centered cubic (FCC) crystals exhibit twelve slip systems, compare, for example, Hull [16]. The plastic strain ε_p is related to the plastic slips γ_ξ and is assumed to be expressed by

$$\varepsilon_p = \sum_{\xi=1}^{N} \gamma_\xi \frac{1}{2}(d_\xi \otimes n_\xi + n_\xi \otimes d_\xi) = \sum_{\xi=1}^{N} \gamma_\xi M_\xi, \tag{2}$$

compare, for example, [17]. The plastic slip γ_ξ is defined for $\xi = 1, \ldots, N$ active slip systems. Here, M_ξ denotes the Schmid tensor of slip system ξ. The accumulated plastic slip γ_{ac} is defined by its rate as the sum of the plastic slip rate in each slip system $\dot{\gamma}_{ac} = \sum_{\xi=1}^{N} |\dot{\gamma}_\xi|$, compare, for example, [17]. For a slip system ξ, the projection of the Cauchy stress and the Schmid tensor yields the resolved shear stress τ_ξ with $\tau_\xi = \sigma \cdot M_\xi$. The initial value of the critical resolved shear stress τ_C can be regarded as a fixed material property. However, the critical yield stress increases due to hardening, compare, for example, Kocks and Mecking [18]. The considered flow rule for the individual plastic slips, and the critical resolved shear stress τ_C, describing an isotropic hardening of Voce type, reads

$$\dot{\gamma}_\xi = \dot{\gamma}_0 \, \text{sgn}(\tau_\xi) \left\langle \frac{|\tau_\xi| - \tau_C}{\tau_D} \right\rangle^m, \qquad \tau_C(\gamma_{ac}) = \tau_\infty - (\tau_\infty - \tau_0) \exp\left(\frac{-\Theta_0}{\tau_\infty - \tau_0} \gamma_{ac} \right), \tag{3}$$

compare, for example, Wulfinghoff [19] and Bayerschen [20], respectively. Herein, τ_D denotes a positive drag stress, the strain rate sensitivity is defined as m, and the referential shear rate is given by $\dot{\gamma}_0$. The Macauley brackets are defined as $\langle a \rangle = \max(a, 0)$, that is, an argument of non-negativity is ensured. The initial yield stress is referred to as τ_0, whereas the saturation yield stress is denoted by τ_∞, and Θ_0 represents the initial hardening modulus. The framework presented constitutes a thermomechanically weakly coupled theory, compare the discussion by Prahs et al. [21].

3 | MULTIPHASE-FIELD METHOD

Free energy functional

The free energy functional $\mathcal{F}$, as used in the work at hand, depends on an N^*-tuple of order parameters $\boldsymbol{\phi} = \{\phi_1, \ldots, \phi_{N^*}\}$ with $\alpha = 1, \ldots, N^*$ phases, its gradients $\nabla\boldsymbol{\phi} = \{\nabla\phi_1, \ldots, \nabla\phi_{N^*}\}$, and the displacement $\boldsymbol{u}$, and reads

$$\mathcal{F}[\boldsymbol{\phi}, \nabla\boldsymbol{\phi}, \boldsymbol{u}] = \int_{\mathcal{V}} f \, dv = \int_{\mathcal{V}} f_{\text{grad}} + f_{\text{pot}} + \bar{f}_{\text{bulk}} \, dv, \quad \text{with} \quad \bar{f}_{\text{bulk}} = \bar{f}_e + \bar{f}_p \tag{4}$$

compare, for example, Nestler et al. [22]. Here, the interface contribution consists of the gradient and potential energy density f_{grad} and f_{pot}, respectively. The contributions from the bulk are denoted by $\bar{f}_{\text{bulk}}$ and are given by an elastic $\bar{f}_{\text{e}}$ and a plastic energy density $\bar{f}_{\text{p}}$. The gradient energy density f_{grad} and the multi-obstacle potential f_{pot} are written as

$$f_{\text{grad}}(\boldsymbol{\phi}, \nabla \boldsymbol{\phi}) = \epsilon \sum_{\alpha, \beta > \alpha}^{N^*} \gamma_{\alpha\beta} |\phi_\alpha \nabla \phi_\beta - \phi_\beta \nabla \phi_\alpha|^2, \quad f_{\text{pot}}(\boldsymbol{\phi}) = \frac{16}{\epsilon \pi^2} \sum_{\alpha < \beta}^{N^*} \gamma_{\alpha\beta} \phi_\alpha \phi_\beta + \frac{1}{\epsilon} \sum_{\alpha < \beta < \delta}^{N^*} \gamma_{\alpha\beta\delta} \phi_\alpha \phi_\beta \phi_\delta, \tag{5}$$

compare, for example, Nestler et al. [22]. If the N^*-tuple $\boldsymbol{\phi}$ is not within the Gibbs-simplex, given by $\mathcal{G} = [\boldsymbol{\phi}| \sum_{\alpha=1}^{N^*} \phi_\alpha(\boldsymbol{x}, t) = 1, \ \phi_\alpha \geq 0 \ \forall \alpha]$, compare, for example, Schneider et al. [23], $f_{\text{pot}} = \infty$ is enforced. The interfacial energy between phases α and β is denoted by $\gamma_{\alpha\beta}$ and is for simplicity assumed to be isotropic, that is, not dependent on the crystal orientation. Formation of third phases in a two-phase region are prevented using the term related to $\gamma_{\alpha\beta\delta}$, compare, for example, Nestler et al. [22]. The parameter ϵ is related to the width of the interface l. The width of an interface in equilibrium l_{eq} is given by $l_{\text{eq}} = \epsilon \pi^2/4$. Each component of the tuple of order parameters ϕ_α is assigned to a phase in the sense of a subregion $\mathcal{V}_\alpha$ of region $\mathcal{V}$. The interpretation of the order parameters as volume fractions yields the summation constraint $\sum_{\alpha=1}^{N^*} \phi_\alpha(\boldsymbol{x}, t) = 1, \forall \boldsymbol{x} \in \mathcal{V}, t \geq 0$, compare, for example, Nestler et al. [22].

Phase-specific bulk energy densities

In the work at hand, the implementation of CP within the diffuse interface is based on the jump condition approach, compare, for example, Refs. [9–11], as introduced and described in detail by Prahs et al. [12]. Thereby, the balance of linear momentum at a singular surface and the Hadamard jump condition are satisfied at each point within the diffuse interface. Each phase can be associated with its own constitutive behavior and specific grain orientation, in the context of crystalline microstructures. The phase-specific elastic free energy density f_{e}^α is formulated as

$$f_{\text{e}}^\alpha \left(\varepsilon^\alpha(\boldsymbol{\phi}) - \varepsilon_{\text{p}}^\alpha \right) = \frac{1}{2} \left(\varepsilon^\alpha(\boldsymbol{\phi}) - \varepsilon_{\text{p}}^\alpha \right) \cdot \left(\mathbb{C}^\alpha [\varepsilon^\alpha(\boldsymbol{\phi}) - \varepsilon_{\text{p}}^\alpha] \right), \tag{6}$$

compare, for example, Herrmann et al. [8]. Herein, $\mathbb{C}^\alpha$ denotes the phase-specific stiffness tensor. The interpolation of the phase-specific elastic free energies f_{e}^α yields the elastic free energy density $\bar{f}_{\text{e}} = \sum_\alpha \phi_\alpha f_{\text{e}}^\alpha$, compare, for example, Herrmann et al. [8]. The balance of linear momentum is formulated in the terms of the interpolated stress tensor $\bar{\boldsymbol{\sigma}}$. It can be derived by minimizing the free energy functional $\mathcal{F}$, compare Equation (4), with respect to the displacement $\boldsymbol{u}$ reading $\text{div}(\bar{\boldsymbol{\sigma}}) = \boldsymbol{0}$, with $\bar{\boldsymbol{\sigma}} = \sum_{\alpha=1}^{N^*} \phi_\alpha \boldsymbol{\sigma}^\alpha$, compare, for example, Prahs et al. [12]. Within the phase-specific plastic field approach, the plastic energy density $\bar{f}_{\text{p}}$ is given by the interpolation of the phase-specific plastic fields f_{p}^α, reading $\bar{f}_{\text{p}} = \sum_{\alpha=1}^{N^*} \phi_\alpha f_{\text{p}}^\alpha$, compare, for example, Prahs et al. [12]. As pointed out above, each phase can be associated with specific material properties and specific grain orientations. Therefore, a phase-specific plastic energy density can be derived from $\tau_{\text{C}}^\alpha = \partial f_{\text{p}}^\alpha / \partial \gamma_{\text{ac}}^\alpha + \tau_0^\alpha$, compare, for example, Prahs et al. [12], reading
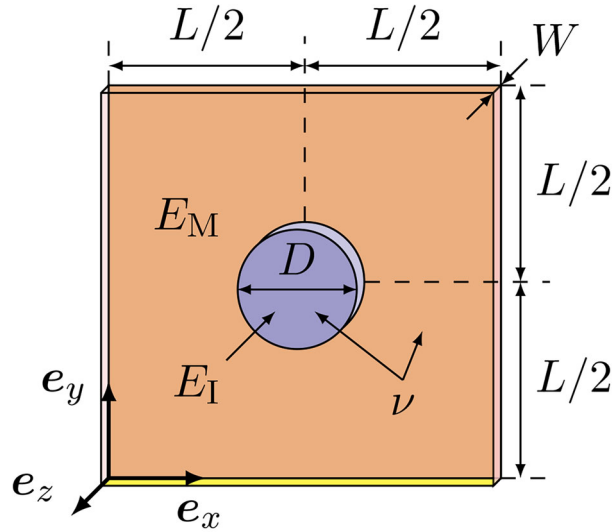
$$f_{\text{p}}^\alpha(\gamma_{\text{ac}}^\alpha) = (\tau_\infty^\alpha - \tau_0^\alpha)\gamma_{\text{ac}}^\alpha + \frac{(\tau_\infty^\alpha - \tau_0^\alpha)^2}{\Theta_0^\alpha} \exp\left(\frac{-\Theta_0^\alpha}{\tau_\infty^\alpha - \tau_0^\alpha} \gamma_{\text{ac}}^\alpha \right) - \frac{(\tau_\infty^\alpha - \tau_0^\alpha)^2}{\Theta_0^\alpha} \tag{7}$$

which applies for the bulk and the diffuse interfaces, compare, for example, Prahs et al. [12]. The condition $f_{\text{p}}^\alpha(\gamma_{\text{ac}}^\alpha = 0) = 0$ is met, by introducing an integration constant $C^\alpha = -(\tau_\infty^\alpha - \tau_0^\alpha)^2 / \Theta_0^\alpha$. Thus, a nonvanishing plastic energy density arises only for $\gamma_{\text{ac}}^\alpha > 0$.

Evolution equation of order parameters

The free energy functional, compare Equation (4), is minimized by the evolution of the phases. Amongst other approaches, the evolution can be derived using a superposition of pairwise interactions of $\tilde{N}$ locally present phases, compare [24]. The evolution equation of order parameters, as used in the work at hand, reads

$$\frac{\partial \phi_\alpha}{\partial t} = -\frac{1}{\tilde{N}\epsilon} \sum_{\beta \neq \alpha}^{\tilde{N}} \left[M_{\alpha\beta} \left(\frac{8\sqrt{\phi_\alpha \phi_\beta}}{\pi} \Delta_{\text{bulk}}^{\alpha\beta} + \Delta_{\text{intf}}^{\alpha\beta} + \Delta_{\text{acurv}}^{\alpha\beta} \right) \right], \tag{8}$$

FIGURE 2 Schematic representation of the quasi two-dimensional simulation domain with a cylindrical inclusion, the inhomogeneity, and the corresponding geometrical dimensions.

compare Schoof et al. [25]. Here, $M_{\alpha\beta}$ denotes the mobility of the interface between phases α and β. The bulk driving force, given as $\Delta_{\text{bulk}}^{\alpha\beta} := \partial \bar{f}_{\text{bulk}} / \partial \phi_{\alpha} - \partial \bar{f}_{\text{bulk}} / \partial \phi_{\beta}$, simplifies to

$$\Delta_{\text{bulk}}^{\alpha\beta} = \{f_e\}^{\alpha\beta} + \{f_p\}^{\alpha\beta} - \bar{\sigma} \cdot \left([H]^{1\beta} - [H]^{1\alpha} \right), \tag{9}$$

as derived in detail by Prahs et al. [12]. Herein, the jump of a quantity ψ across a diffuse interface between two phases α and β is expressed by $\{\psi\}^{\alpha\beta} = \psi^{\alpha} - \psi^{\beta}$. The surface driving force $\Delta_{\text{intf}}^{\alpha\beta}$ yields

$$\Delta_{\text{intf}}^{\alpha\beta} := \frac{\partial f_{\text{grad}} + f_{\text{pot}}}{\partial \phi_{\alpha}} - \frac{\partial f_{\text{grad}} + f_{\text{pot}}}{\partial \phi_{\beta}} - \left(\text{div}\left(\frac{\partial f_{\text{grad}}}{\partial \nabla \phi_{\alpha}} \right) - \text{div}\left(\frac{\partial f_{\text{grad}}}{\partial \nabla \phi_{\beta}} \right) \right), \tag{10}$$

compare Prahs et al.[12]. The term $\Delta_{\text{acurv}}^{\alpha\beta}$ is similar to the surface driving force $\Delta_{\text{intf}}^{\alpha\beta}$, but it is formulated in normal direction of the interface only. Moreover, it is not associated with the surface energy $\gamma_{\alpha\beta}$ and instead dependent on a numerical parameter γ^c, compare, for example, Schoof et al. [26]. The formulation of Equation (10) in normal direction yields $\Delta_{\text{acurv}}^{\alpha\beta}$, which induces no curvature minimization. The combination of the interface terms, compare, for example, Schoof et al. [26], allows to create a stable interface, where $\Delta_{\text{acurv}}^{\alpha\beta}$ does not contribute to curvature minimization, while $\Delta_{\text{intf}}^{\alpha\beta}$ accounts for a surface energy $\gamma_{\alpha\beta}$ inducing curvature minimization. The stability of the interface is affected by the ratio of interface energy densities and surface energy densities and can be adjusted by means of the numerical parameter γ^c and the surface energy $\gamma_{\alpha\beta}$ as well as the amount of curvature minimization.

4 | RESULTS

Simulation setup and boundary conditions

For the simulations, a quasi two-dimensional setup is considered with a quadratic domain and an inclusion, called inhomogeneity, in its center, as illustrated in Figure 2. The domain is discretized by $600 \times 600 \times 1$ cells, regarding the $\boldsymbol{e}_x$-, $\boldsymbol{e}_y$-, and $\boldsymbol{e}_z$-direction using an equidistant, Cartesian grid. The domain depth corresponds to the spatial discretization, that is, $W \equiv \Delta z$. The Dirichlet boundary conditions

$$u_x(0, y, z) = -u_x(L, y, z) = -u_0, \quad \text{and} \quad u_y(x, 0, z) = u_y(x, L, z) = u_z(x, y, 0) = u_z(x, y, L) = 0 \tag{11}$$

TABLE 1 Material parameters are chosen corresponding to aluminum as an example for an FCC material, compare, for example, Bertram and Glüge [27]. The indices $(\cdot)_M$ and $(\cdot)_I$ correspond to the matrix and inhomogeneity, respectively. Parameters without index apply to both.

| Parameter	Symbol	Value	Unit
Young's modulus	E_M	78.311	GPa
Poisson's ratio	ν	0.336	-
Initial yield stress	τ_0^M	20.0	MPa
	τ_0^I	80.0	MPa
Saturation yield stress	τ_∞^M	25.0	MPa
	τ_∞^I	88.0	MPa
Initial hardening modulus	Θ_0^M	3.24	GPa
	Θ_0^I	5.52	GPa
Drag stress	τ^D	1.0	MPa
Sensitivity exponent	m	8.0	-
Reference shear rate	$\dot{\gamma}_0$	0.001	s^{-1}

TABLE 2 Numerical and geometrical parameters are adjusted in a parameter study to minimize their impact on the phase evolution. It is pointed out, that in the present work the surface energy $\gamma_{\alpha\beta}$ functions as a numerical parameter.

| Parameter	Symbol	Value	Unit
Width of the domain	L	300.0	μm
Initial inclusion diameter	D	12.0	μm
Cells in the interface	n_{intf}	8	-
Spacial discretization	Δx	0.5	μm
Surface energy	$\gamma_{\alpha\beta}$	1.3	mJ m^{-2}
Time discretization	Δt	0.5	s

apply. Here, the Dirichlet boundary condition u_0 is chosen such that $\varepsilon_{xx} = 0.07\%$ holds true at the left and right boundary. No further conditions regarding the displacement field are imposed on the boundary. Regarding the field of order parameters, Neumann boundary conditions apply on all six sides, that is, $\partial\phi_\alpha/\partial x_i = 0 \; \forall x_i \in \partial\mathcal{B}_i$. Here, $\partial\mathcal{B}_i$ represents the boundary with the corresponding normal direction i. The initial diameter of the inhomogeneity D is chosen sufficiently small relative to the domain width L, such that the shape of the growing inhomogeneity exhibits an equilibrium, before boundary effects are present. The matrix is considered to exhibit an elasto-plastic behavior and subject to hardening of Voce type, as described above. The inhomogeneity has a smaller Young's modulus than the matrix, that is, $E_I < E_M$, and is modeled as elastic, by increasing its initial yield stress τ_0^I sufficiently high. The material parameters, summarized in Table 1, are chosen as an example for an FCC material, mimicking aluminum. The numerical, and geometrical parameters, as summarized in Table 2, are adjusted within a parameter study in order to keep their effect on the phase evolution to a minimum. The interface parameter ϵ is computed based on the width of an interface l_{eq} in equilibrium. The mobility $M_{\alpha\beta}$ is computed dependent on the spatial and time discretization, as well as on surface energy terms, via $1/M_{\alpha\beta} = (4\Delta t(\gamma_{\alpha\beta} + \gamma^c))/(\Delta x)^2$, ensuring numerical stability of the interface, compare, for example, Schoof [28]. The simulations are carried out using dimensionless parameters.

Shape evolution
In the context of quartz and sand, methods to measure and quantify the shape of particles are derived. By Wadell [29], the degree of sphericity is described as the ratio of the surface area of a sphere of the same volume and the actual measured surface area (denoted by subscript O). In the quasi two-dimensional simulations in the work at hand, the circularity $\Psi_{2D} = \sqrt{4\pi A_O}/U_O$, with the circumference of a circle $U(r) = 2\pi r$ and the radius $r = \sqrt{A_O/\pi}$ derived from the actual measured surface area A_O, is used to evaluate the shape of the inhomogeneity. Triggered by the external load, the inhomogeneity starts to grow and simultaneously its shape evolves. In order to compare shapes of different volumes independent of the growth rate, the radius of a circle with an equivalent surface area, referred to as the equivalent radius, is introduced.
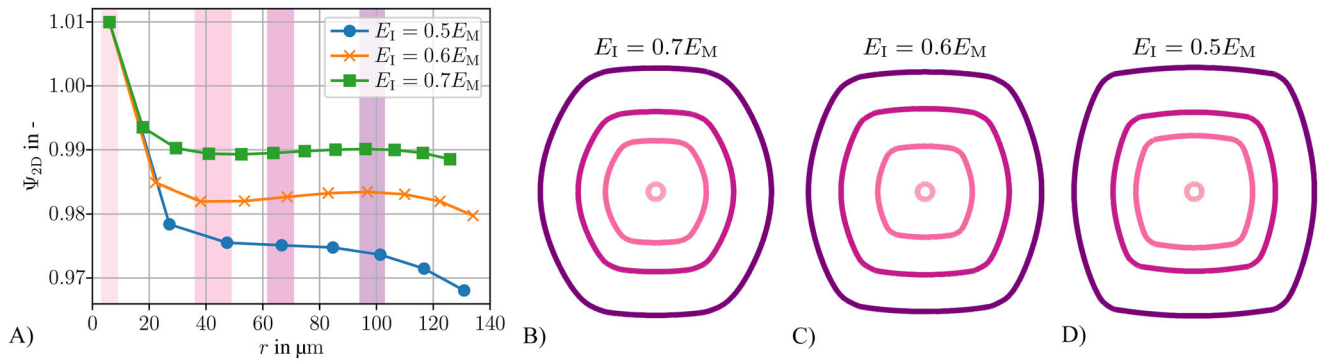
FIGURE 3 Impact of ratio E_I/E_M on the shape of the inhomogeneity. The circularity Ψ_{2D} is plotted against the radius r of a circle with an equivalent surface area (A). In (B–D), the corresponding shapes of the inhomogeneity are illustrated using the corresponding sharp interface for the initial inhomogeneity ($r = 6\,\mu$m) and in equilibrium with approximately $r \in [40, 70, 100]\,\mu$m, which are highlighted by the vertical stripes in A.
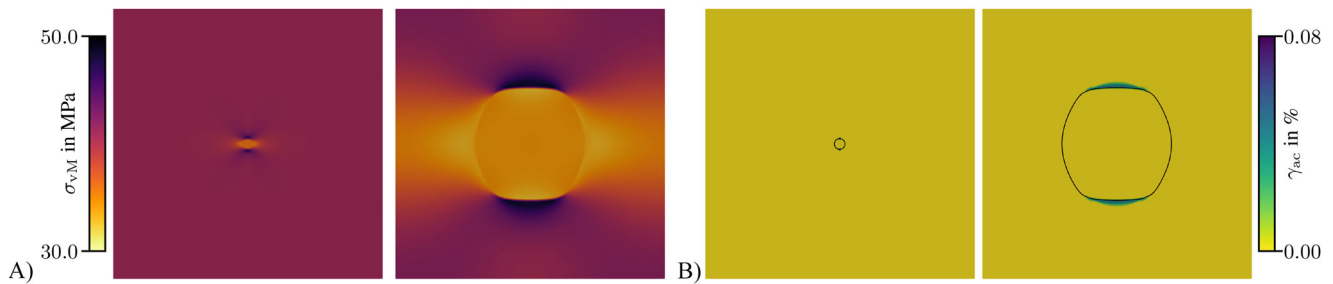
FIGURE 4 Mises stress $\sigma_{vM} = \sqrt{3/2\|\boldsymbol{\sigma}'\|^2}$ (in A) and accumulated plastic slip $\gamma_{ac} = \sum_{\alpha=1}^{N} \phi_\alpha \gamma_{ac}^\alpha$ (in B) of an inhomogeneity with a ratio of the Young's moduli $E_I/E_M = 0.7$. On the left and right side in each subfigure, the initial state and an equilibrium state with $r \approx 70\,\mu$m is displayed, respectively. The black line illustrates the location of the corresponding sharp interface.

An equilibrium shape of the growing inhomogeneity can be identified by a constant circularity Ψ_{2D} over an increasing equivalent radius r. The influence of the Young's moduli related to the inhomogeneity and the matrix is investigated by the ratio E_I/E_M. The Young's modulus of the inhomogeneity is varied with $E_I = \alpha E_M$ with $\alpha \in [0.7, 0.6, 0.5]$. In Figure 3A, the circularity of the growing inhomogeneity is plotted against the equivalent radius. Following the initial shape evolution, the circularity of the inhomogeneity reaches a plateau, that is, an equilibrium shape, before it decreases further due to boundary effects. It is pointed out, that for small inclusion diameters at the simulation start, the resolution is too coarse to compute the circumference U accurately, as a circularity $\Psi_{2D} > 1$ indicates. However, the inhomogeneity grows and reaches equilibrium for much larger radii, where the resolution is sufficient and the circularity can be determined accurately. A greater difference of the Young's moduli results in a smaller circularity in equilibrium, that is, in a greater extent of shape evolution. Thus, it can be concluded, that the difference of the Young's moduli coincides with the deviation of the shape from the initial circular shape. The corresponding shapes of four different time steps and three different ratios of the Young's moduli are illustrated in Figure 3B–D. Depicted are the shape of the initial inhomogeneity ($r = 6\,\mu$m), and the shapes of the inhomogeneity in equilibrium at three different time steps, as highlighted by the vertical stripes in Figure 3A, that is, shapes with approximately equivalent circularity. Again, it can be seen that the equilibrium shape of an inhomogeneity with a greater difference of the Young's moduli is less circular, compare Figure 3D, than with a smaller difference, compare Figure 3B.

The corresponding stress fields for the case of a ratio of $E_I/E_M = 0.7$ are displayed in Figure 4A, on the left representing the beginning of phase evolution and on the right for an inhomogeneity with an equivalent radius of $r \approx 70\,\mu$m. The stress within the inhomogeneity is approximately constant and smaller with respect to the matrix. The corresponding accumulated plastic slip fields are depicted in Figure 4B. It can be seen, that plastic slip occurs in the matrix close to the top and bottom of the inhomogeneity. The bulk driving force acting on the interface is affected by the accumulated plastic slip, explaining the flattened shape.

5 | CONCLUSION

Prahs et al. [12] presented an implementation of a small strain CP theory regarding the diffuse interface region and the bulk material accounting for phase-specific fields and the mechanical jump condition. In the work at hand, their model is applied to investigate the phase evolution of an elastic inclusion, referred to as inhomogeneity, within an elasto-plastic matrix. The shape of the inhomogeneity is significantly influenced by the distribution of the plastic slip. The difference of the elastic properties, that is, the Young's moduli, has a direct influence on the shape of the inhomogeneity in equilibrium. A greater difference of Young's moduli results in a smaller circularity of the inhomogeneity, that is, a greater deviation of the shape from the initial circular shape, and vice versa. Equilibrium shapes can be identified for inclusions with varying volume. Here, the volume of the inclusion increases. The steady growth is induced by elastic fields, that is, due to the nonvanishing Dirichlet boundary conditions at the left and right boundary. In an equilibrium state, two inclusions of different equivalent radius are similar, that is, they have the same shape. If a growing inclusion exhibits a constant circularity, its shape is called equilibrium shape.

ORCID
Thea Kannenberg https://orcid.org/0009-0002-5243-5164

REFERENCES
1. Prahs, A., & Böhlke, T. (2019). On interface conditions on a material singular surface. *Continuum Mechanics and Thermodynamics*, *32*(5), 1417–1434.
2. Moelans, N., Blanpain, B., & Wollants, P. (2008). An introduction to phase-field modeling of microstructure evolution. *Calphad*, *32*(2), 268–294.
3. Steinbach, I. (2009). Phase-field models in materials science. *Modelling and Simulation in Materials Science and Engineering*, *17*(7), 073001.
4. Nestler, B., & Choudhury, A. (2011). Phase-field modeling of multi-component systems. *Current Opinion in Solid State and Materials Science*, *15*(3), 93–105.
5. Asaro, R. J. (1983). Crystal plasticity. *Journal of Applied Mechanics*, *50*(4b), 921–934.
6. Ammar, K., Appolaire, B., Cailletaud, G., & Forest, S. (2009). Combining phase field approach and homogenization methods for modelling phase transformation in elastoplastic media. *European Journal of Computational Mechanics*, *18*(5-6), 485–523.
7. de Rancourt, V., Ammar, K., Appolaire, B., & Forest, S. (2016). Homogenization of viscoplastic constitutive laws within a phase field approach. *Journal of the Mechanics and Physics of Solids*, *88*, 291–319.
8. Herrmann, C., Schoof, E., Schneider, D., Schwab, F., Reiter, A., Selzer, M., & Nestler, B. (2018). Multiphase-field model of small strain elasto-plasticity according to the mechanical jump conditions. *Computational Mechanics*, *62*(6), 1399–1412.
9. Durga, A., Wollants, P., & Moelans, N. (2013). Evaluation of interfacial excess contributions in different phase-field models for elastically inhomogeneous systems. *Modelling and Simulation in Materials Science and Engineering*, *21*(5), 055018.
10. Mosler, J., Shchyglo, O., & Hojjat, H. M. (2014). A novel homogenization method for phase field approaches based on partial rank-one relaxation. *Journal of the Mechanics and Physics of Solids*, *68*, 251–266.
11. Schneider, D., Schwab, F., Schoof, E., Reiter, A., Herrmann, C., Selzer, M., Böhlke, T., & Nestler, B. (2017). On the stress calculation within phase-field approaches: A model for finite deformations. *Computational Mechanics*, *60*(2), 203–217.
12. Prahs, A., Schöller, L., Schwab, F. K., Schneider, D., Böhlke, T., & Nestler, B. (2023). A multiphase-field approach to small strain crystal plasticity accounting for balance equations on singular surfaces. Accepted in Computational Mechanics.
13. Liu, I. S. (2002). *Continuum mechanics*. Springer.
14. Svendsen, B. (2001). Formulation of balance relations and configurational fields for continua with microstructure and moving point defects via invariance. *International Journal of Solids and Structures*, *38*(6-7), 1183–1200.

15. Prahs, A., & Böhlke, T. (2019). On invariance properties of an extended energy balance. *Continuum Mechanics and Thermodynamics*, *32*(3), 843–859.

16. Hull, D. (2001). *Introduction to dislocations*. Butterworth-Heinemann.

17. Albiez, J., Erdle, H., Weygand, D., & Böhlke, T. (2019). A gradient plasticity creep model accounting for slip transfer/activation at interfaces evaluated for the intermetallic NiAl-9mo. *International Journal of Plasticity*, *113*, 291–311.

18. Kocks, U., & Mecking, H. (2003). Physics and phenomenology of strain hardening: The FCC case. *Progress in Materials Science*, *48*(3), 171–273.

19. Wulfinghoff, S. (2014). Numerically efficient gradient crystal plasticity with a grain boundary yield criterion and dislocation-based work-hardening. *Schriftenreihe Kontinuumsmechanik im Maschinenbau* (Vol. 5). KIT Scientific Publishing.

20. Bayerschen, E. (2017). Single-crystal gradient plasticity with an accumulated plastic slip: Theory and applications. *Schriftenreihe Kontinuumsmechanik im Maschinenbau* (Vol. 9). KIT Scientific Publishing.

21. Prahs, A., Reder, M., Schneider, D., & Nestler, B. (2023). Thermomechanically coupled theory in the context of the multiphase-field method. *International Journal of Mechanical Sciences*, *257*, 108484.

22. Nestler, B., Garcke, H., & Stinner, B. (2005). Multicomponent alloy solidification: Phase-field modeling and simulations. *Physical Review E*, *71*(4), 041609.

23. Schneider, D., Schoof, E., Tschukin, O., Reiter, A., Herrmann, C., Schwab, F., Selzer, M., & Nestler, B. (2017). Small strain multiphase-field model accounting for configurational forces and mechanical jump conditions. *Computational Mechanics*, *61*(3), 277–295.

24. Steinbach, I., Pezzolla, F., Nestler, B., Seeßelberg, M., Prieler, R., Schmitz, G., & Rezende, J. (1996). A phase field concept for multiphase systems. *Physica D: Nonlinear Phenomena*, *94*(3), 135–147.

25. Schoof, E., Herrmann, C., Streichhan, N., Selzer, M., Schneider, D., & Nestler, B. (2019). On the multiphase-field modeling of martensitic phase transformation in dual-phase steel using J_2-viscoplasticity. *Modelling and Simulation in Materials Science and Engineering*, *27*(2), 025010.

26. Schoof, E., Schneider, D., Streichhan, N., Mittnacht, T., Selzer, M., & Nestler, B. (2018). Multiphase-field modeling of martensitic phase transformation in a dual-phase microstructure. *International Journal of Solids and Structures*, *134*, 181–194.

27. Bertram, A., & Glüge, R. (2015). *Solid mechanics*. Springer International Publishing.

28. Schoof, E. (2021). Chemomechanische Modellierung der Wärmebehandlung von Stählen mit der Phasenfeldmethode. *Schriftenreihe des Instituts für Angewandte Materialien*. Band 93. KIT Scientific Publishing.

29. Wadell, H. (1935). Volume, shape, and roundness of quartz particles. *The Journal of Geology*, *43*(3), 250–280.